



Magnetic field assisted synthesis of dense braided rope NiCoP as a highly efficient hydrogen evolution electrocatalyst

Zhong Wang^{a,e}, Shuang Yuan^{a,c,e,*}, Hao Tian^a, Tuo Zang^a, Jinyang Li^a, Jiaqi Liu^{a,e}, Guojian Li^d, Jun Wang^b, Tie Liu^d, Qiang Wang^{d,**}

^a School of Metallurgy, Northeastern University, Shenyang 110819, China

^b State Key Laboratory of Solidification Processing, Northwestern Polytechnical University, Xi'an 710072, China

^c Key Laboratory for Ecological Metallurgy of Multimetallurgical Mineral (Ministry of Education), Northeastern University, Shenyang 110819, China

^d Key Laboratory of Electromagnetic Processing of Materials (Ministry of Education), Northeastern University, Shenyang 110819, China

^e Engineering Research Center of Frontier Technologies for Low-carbon Steelmaking (Ministry of Education), Liaoning Low-carbon Steelmaking Technology Engineering Research Center, Shenyang 110819, China

ARTICLE INFO

Keywords:

Magnetic field
Hydrogen evolution reaction
Magnetohydrodynamic
High catalytic activity

ABSTRACT

The design of efficient stable and noble metal-free catalysts for the hydrogen evolution reaction is an important and challenging global task. In this work, high catalytic activity NiCoP braided rope was prepared by magneto-electrodeposition strategy for the first time. Notably, the magnetic field-induced magnetohydrodynamic effect serves multiple purposes. COMSOL numerical simulations reveal the formation mechanism of a braided rope structure. Density functional theory (DFT) calculations confirm that NiCoP has superior activity, attributed to Co active sites. In 1.0 M KOH and 0.5 M H₂SO₄, respectively, the overpotential of NiCoP prepared under 600 mT magnetic field (NiCoP-600) is only 48 and 34 mV at a current density of 10 mA cm⁻². Additionally, the TOF of NiCoP-600 was 36 times as high as that of NiCoP at an overpotential of 100 mV. Furthermore, NiCoP-600 can be used as the cathode and anode for overall water splitting in an alkaline electrolyzer.

1. Introduction

Because of limited resources and environmental pollution associated with the use of fossil fuels, there is an urgent need to develop new clean energy resources [1–3]. Hydrogen has the characteristics of high energy density and being renewable and environmental friendly, which make it an ideal substitute for fossil fuels [4–7]. However, in the hydrolysis process, the activity and stability of the catalyst determine the overpotential needed to overcome the poor reaction kinetics. For example, Pt, Pd, and their alloys and compounds show high hydrogen evolution reaction (HER) activity, which results in the dissociation of water at low potentials [8,9]. However, from a commercial viewpoint, the high cost and scarcity of these materials greatly limit their large-scale applications [10,11]. Therefore, to promote a hydrogen energy economy and address the energy crisis, there is an urgent need to develop non-noble metal catalysts with low cost and abundant storage ability.

Transition metal phosphides (TMPs) have been widely reported as HER catalysts in recent years [12–15]. The P atom in TMPs can strongly

interact with H atoms, which weakens the binding energy between the transition metal and the H atom, thus promoting adsorption and desorption at active sites [16–18]. However, TMPs undergo destabilization and structural reconstruction during the reaction process, resulting in kinetic retardation of the electrocatalytic reaction, which has greatly limited the further development of TMPs. The performance of HER should be optimized without changing the composition of TMP elements; hence, two important factors should be considered. First, regulation of the metal ratio in the TMP to expose more active sites. Gupta et al. [19] determined the optimal Ni/(Ni+Co) ratio for HER performance by changing the concentration of cobalt and nickel salts in the solution. Chen et al. [20] melted FeCoNi with different weight ratios in an induction furnace and explored the influence of different elemental composition ratios on the catalytic performance of the electrodes. Another important factor is to prepare special morphologies and structures to avoid structural collapse and agglomeration during catalyst stability testing. Shen et al. [21] synthesized a dense nanosheet array [Ru/Co(OH)₂] on the surface of carbon cloth (CC) by electrodeposition.

* Corresponding author at: School of Metallurgy, Northeastern University, Shenyang 110819, China.

** Corresponding author.

E-mail addresses: yuan@smm.neu.edu.cn (S. Yuan), wangq@epm.neu.edu.cn (Q. Wang).

The dense structure promoted mass transport and bubble detachment while maintaining strong stability at a current density of 500 mA cm^{-2} . Song et al. [22] used a hydrothermal method to cover the surface of a nickel foam with rod-shaped Co-P nano-arrays; the morphology of the resulting catalysts did not change during long-term stability testing. Although, some progress has been achieved by traditional preparation methods, these approaches are not capable of controlling the specific structure and content at the same time.

In recent years, the morphology, structure, and elemental content of catalysts synthesized regulation under by magnetic fields have been explored [23–27]. Among various synthetic methods, the coupling of magnetic fields and electrodeposition is a promising method [28–31]. The magnetohydrodynamic (MHD) effect induced by magneto-electrodeposition (MED) can optimize the heterogeneous deposition, particle agglomeration, and stacking growth of metal elements. Li et al. [32] reported that MED not only constructed 3D cross-linked nested $\text{Ti}_3\text{C}_2\text{T}_x/\text{NiCo-LDH}$ on the CC surface but also increased the loading of active sites. Wei et al. [33] confirmed that a magnetic field increases the deposition rate of Cu, and pointed out that the enhancement mechanism derives from convection caused by a Lorentz force, which reduces the thickness of the Cu diffusion layer and increases the mass transfer.

In this work, high activity NiCoP was grown on carbon paper (CP) using the MED method, and the obtained catalyst was used directly as a self-supporting integrated electrode. Notably, for NiCoP prepared under a 600 mT magnetic field, the Ni/Co ratio was adjustable, enabling optimization of the charge distribution of the catalysts. Additionally, the MHD effect caused by a magnetic field is a key factor contributing to the formation of dense braided rope structures. Thus, NiCoP-600 exhibited HER activity comparable to that of precious metal Pt catalysts under alkaline or acidic conditions. In 1.0 M KOH and 0.5 M H_2SO_4 the overpotential was only 48 and 34 mV, respectively, at a current density of 10 mA cm^{-2} , and the Tafel slope was relatively small at 54 and 48 mV dec^{-1} . Additionally, NiCoP-600 showed excellent durability in long-term stability tests. This simple, clean, and contactless MED technology will open new avenues for research into material content control and structural design.

2. Experimental section

2.1. Material preparation

Carbon paper (CP, TGP-H-060), nitric acid (HNO_3 , 30 %), ethanol ($\text{C}_2\text{H}_5\text{OH}$), nickel chloride hexahydrate ($\text{NiCl}_2 \cdot 6\text{H}_2\text{O}$), cobalt chloride hexahydrate ($\text{CoCl}_2 \cdot 6\text{H}_2\text{O}$), ammonium chloride (NH_4Cl), sodium hypophosphite ($\text{NaH}_2\text{PO}_2 \cdot 2\text{H}_2\text{O}$), and deionized water (H_2O). The above raw materials were all obtained from Shanghai Aladdin Reagent Co., Ltd. Potassium hydroxide (KOH) and sulfuric acid (H_2SO_4) were from Sinopharm Chemical Reagent Co., Ltd. The nitrogen (N_2 , 99 %) and oxygen (O_2 , 99 %) used in the experiment were obtained from Dalian Kerun Special Gas Co., Ltd.

2.2. Synthesis of NiCoP and NiCoP-600

NiCoP was synthesized by one-step electrodeposition. First, the CP was cut to a specified size and then placed in a water bath in a nitric acid solution at 50°C . The purpose of this step was to increase the oxygen-containing functional groups, such as hydroxyl and carboxyl groups, on the surface of the CP. After washing repeatedly with deionized water and absolute ethanol and drying in a vacuum box after cleaning, hydrophilic carbon paper (H-CP) was finally obtained. Then, 2 mmol $\text{NiCl}_2 \cdot 6\text{H}_2\text{O}$, 2 mmol $\text{CoCl}_2 \cdot 6\text{H}_2\text{O}$, 5 mmol NH_4Cl , and 5 mmol $\text{NaH}_2\text{PO}_2 \cdot 2\text{H}_2\text{O}$ were dissolved in 50 mL of deionized water and stirred uniformly for 30 min with a magnetic stirrer to form an electrodeposition solution. H-CP was used as the working electrode, a platinum sheet as the counter electrode, and a saturated calomel electrode as the reference

electrode to construct a three-electrode system. The cell was then placed in a magnetic field (0, 300 and 600 mT) at a specified temperature (Fig. S1). The deposition parameter was maintained at a constant potential of -1 V for 30 min. After the electrodeposition, the surface of the products was repeatedly rinsed using deionized water and anhydrous ethanol to obtain NiCoP, NiCoP-300, and NiCoP-600.

Furthermore, NiCoP, Ni-P, Co-P, and Ni-Co were prepared using similar procedures. The composition of Ni-P was based on 2 mmol $\text{NiCl}_2 \cdot 6\text{H}_2\text{O}$, 5 mmol NH_4Cl and 5 mmol $\text{NaH}_2\text{PO}_2 \cdot 2\text{H}_2\text{O}$ dissolved in 50 mL of deionized water. The composition of Co-P was based on 2 mmol $\text{CoCl}_2 \cdot 6\text{H}_2\text{O}$, 5 mmol NH_4Cl , and 5 mmol $\text{NaH}_2\text{PO}_2 \cdot 2\text{H}_2\text{O}$ dissolved in 50 mL of deionized water. The composition of Ni-Co was based on 2 mmol $\text{NiCl}_2 \cdot 6\text{H}_2\text{O}$, 2 mmol $\text{CoCl}_2 \cdot 6\text{H}_2\text{O}$, and 5 mmol NH_4Cl dissolved in 50 mL of deionized water. Other steps were consistent with the preparation of NiCoP, to finally obtain Ni-P, Co-P, and Ni-Co.

2.3. Material characterization

The morphology and structure of the NiCoP and NiCoP-600 were characterized with a scanning electron microscope (SEM, S4800 HSD, Hitachi) and a transmission electron microscope (TEM, Tecnai G2 F20, FEI). Energy dispersive X-ray spectroscopy (EDX) was used to study the distribution of Ni, Co, and P elements. Selected area electron diffraction (SAED) was used to determine the crystal properties of materials. X-ray diffraction (XRD, Bruker D8) was used to determine the crystal structure of the samples. X-ray photoelectron spectroscopy (XPS, ESCALAB-250) was used to study the chemical composition and valence states of NiCoP. Brunner-Emmet-Teller (BET, ASIQC0 V602-5) was used to calculate the specific surface area. A vibrating sample magnetometer (VSM, Lake Shore 7404) was used to measure the magnetic properties of the materials. The contents of Ni, Co, and P in NiCoP and NiCoP-600 were determined by ICP-MS (Agilent Technologies 7800). The contact angle was measured in a greenhouse using deionized water and a contact angle measurement system (Data Physics Instruments GmbH, Germany). A high-speed camera was used to capture bubbles generated during electrodeposition at 1000 fps. The diameter of the bubbles produced in the electrodeposition was measured using Image-Pro Plus software.

2.4. Electrochemical measurement

All of the catalysts were tested on an electrochemical workstation (VSP, Bio-Logic). The electrochemical testing was performed in a three-electrode system, in which the working electrode was the prepared catalyst and the counter electrode was a graphite sheet ($5 \times 15 \times 3 \text{ mm}^3$). The reference electrodes were mercuric oxide electrodes (under alkaline conditions) and saturated calomel electrodes (under acidic conditions). A 1.0 M KOH ($\text{pH} = 13.8$) solution was used as the alkaline electrolyte, and 0.5 M H_2SO_4 ($\text{pH} = 0.2$) as the acidic electrolyte. To obtain a stable current, linear sweep voltammetry (LSV) was tested at a sweep rate of 50 mV s^{-1} for 30 cycles and then at a sweep rate of 5 mV s^{-1} . Additionally, all polarization curves were iR -corrected $E_{\text{corr}} = E_{\text{mea}} - iR_s$, where E_{corr} is the iR compensation potential, E_{mea} is the actual measured potential, i is the actual measured current density, and R_s is the equivalent solution resistance measured by electrochemical impedance. The Tafel slope was calculated from the polarization curve. The electric double-layer capacitance in the non-Faraday potential region was measured at cyclic voltammetry (CV) sweep rates of 20, 40, 60, 80, 100, 120, 140, 160, 180, and 200 mV s^{-1} .

3. Results and discussion

As shown in Fig. 1a, the self-supporting NiCoP/CP catalyst was prepared by electrodeposition method. Firstly, CP was placed in 30 % nitric acid solution for hydrophilic treatment (H-CP), and then H-CP was electrodeposited NiCoP with and without a magnetic field. Then, a self-supporting NiCoP/CP catalyst was obtained (Fig. S2). The NiCoP

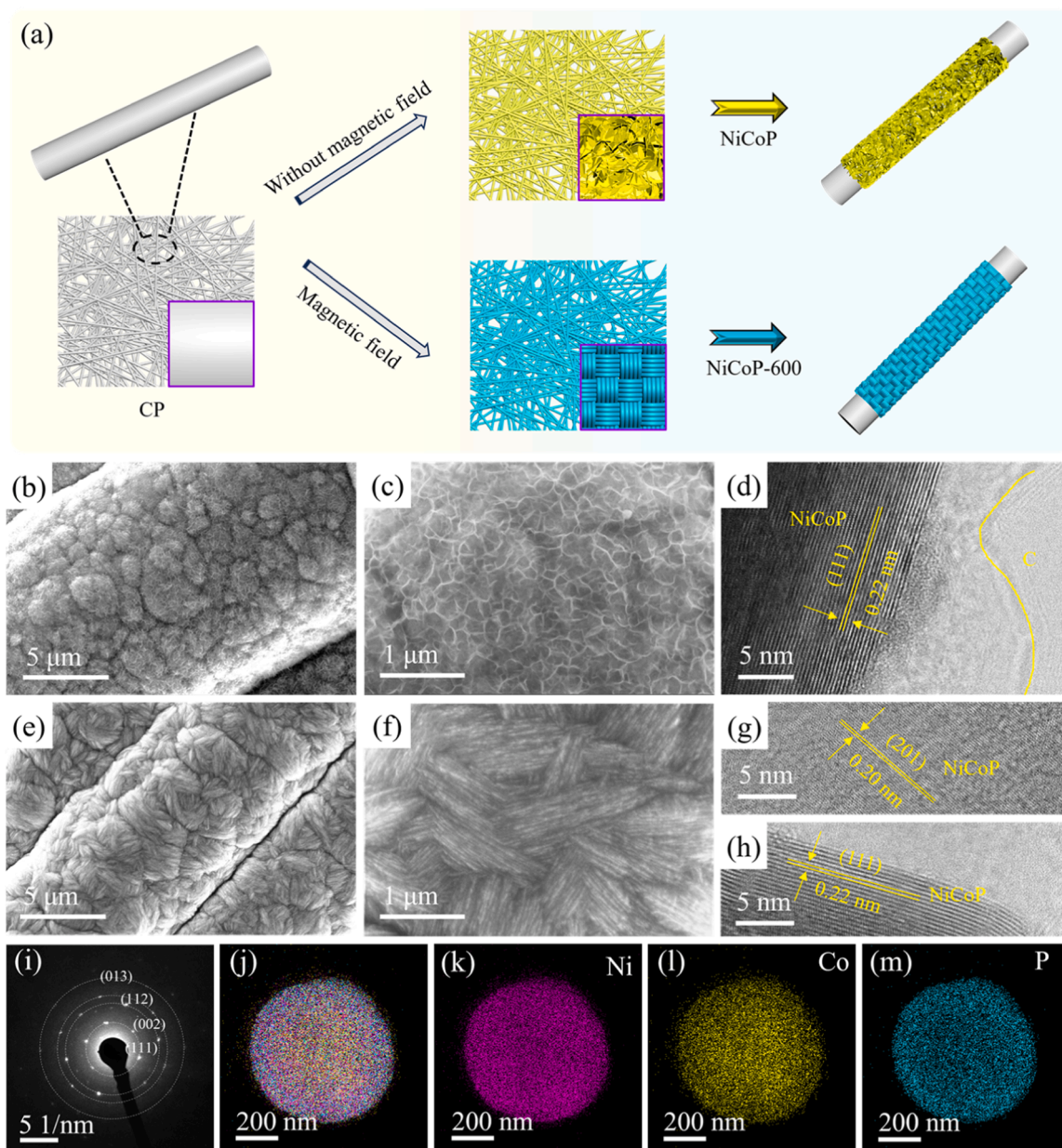


Fig. 1. (a) The schematic for the preparation of NiCoP and NiCoP-600 on carbon paper. (b-c) SEM and (d) HRTEM images of NiCoP. (e-f) SEM, (g-h) HRTEM, (i) SAED, and (j-m) EDX elemental mapping images of NiCoP-600.

prepared without a magnetic field had a flower-shaped surface. Remarkably, when a 600 mT magnetic field was applied, the NiCoP surface formed a dense, braided rope shape. Fig. S3 shows the adsorption-desorption isotherms for CP, NiCoP, and NiCoP-600 with specific surface areas of 1.39, 3.75, and 4.73 m²/g, respectively. Additionally, the deposition yield of NiCoP-600 was improved compared with that of NiCoP, and the yield gradually increased together with the magnetic field intensity (Table S1). To further verify that a magnetic field can improve the deposition yield, Ni-P, Co-P, and Ni-Co were prepared with and without a magnetic field. There is no doubt that the test results show that the application of a magnetic field during electrodepositions can improve the deposition yield (Table S2). Inductively coupled plasma mass spectrometry (ICP-MS) was used to test the element contents in NiCoP and NiCoP-600. The results are shown in Table S3, and the contents of Ni, Co, and P in NiCoP were 24.5 %, 32.6 %, and 2.1 %, respectively. However, the weight percentage of Ni in NiCoP-600 was lower than that of NiCoP at 19.9 %; the weight

percentage of Co was higher than that of NiCoP at 36.2 %, and the content of P was 2.2 %.

The surface morphology of the samples was observed using SEM and TEM. Figs. S4-S5 show SEM images of CP and H-CP, and their surfaces had a nanorod structure, which can provide a large space for deposits. As shown in Fig. 1b-c, the NiCoP surface was composed of nanospheres, which had loose flower-like shapes. High-resolution transmission electron microscope (HRTEM) images of NiCoP are shown in Fig. 1d and S6. Lattice stripes at 0.22 nm correspond to the (111) crystal plane of NiCoP. Additionally, lattice stripes of C appeared, derived from the CP. The corresponding TEM and Energy dispersive X-ray (EDX) elemental mapping images (Fig. S7) showed that the elements Ni, Co, and P were uniformly distributed. To further optimize the HER catalytic activity of NiCoP, Figs. S8-S9 show SEM images of NiCoP formed at different deposition times and deposition potentials. The LSV results (Figs. S10-S11) show that when electrodeposition was performed for a short time or at too low a potential, fewer products were deposited. Conversely, the

sediment covered the porous structure of H-CP, which hindered the detachment of bubbles. Fig. 1e-f and S12-S13 show SEM images of NiCoP-300 and NiCoP-600, and its morphology and structural change from a loose flower rope to a dense braided rope. Additionally, the nanorod diameters of CP, NiCoP, and NiCoP-600 were measured, and their average diameters were 8.2, 11.9, and 10.3 μm , respectively (Fig. S14). However, the diameter of NiCoP-600 was lower than that of NiCoP, which is attributed to its dense braided rope structure. In order to further study the crystal structure and composition of the NiCoP, we scraped the NiCoP off the carbon paper and characterized it by TEM. Obviously, the NiCoP formed clusters during scraping process. Fig. 1g-h and S15 show HRTEM and the EDX spectrum of NiCoP-600, in which the (201) and (111) crystal planes of NiCoP can match the lattice stripes of 0.19 and 0.22 nm (Fig. S16) [34,35], which indicates that the crystal structure of the samples prepared under the magnetic field did not change. The SAED in Fig. 1i shows the polycrystalline properties of NiCoP-600, which matched the crystal orientation of NiCoP in the HRTEM. Fig. 1j-m show the energy-dispersive X-ray spectroscopy results for NiCoP-600. The elements Ni, Co, and P were uniformly distributed

on the surface, which also confirmed the successful preparation of NiCoP.

As shown in Fig. 2a, charged particles tended to gather on the convex surface during electrodeposition without a magnetic field. Over a longer deposition time, the particles stacked along the raised surface to form nanosheets [36]. When the magnetic field was applied, the MHD effect caused by the Lorentz force changed the direction of motion of charged particles and caused them to spiral [37]. Therefore, these charged particles deposited not only on raised surfaces but also around these surfaces, forming a dense braided rope. At the same time, the trajectory distribution of charged particles with and without magnetic field is numerically simulated by COMSOL. As can be seen from Fig. 2b and S17-S19, these charged particles tended to deposit on the convex surface in the absence of a magnetic field. However, when a magnetic field was applied, the particles also deposited around the convex surface.

The deposition yields of Ni-P (from 16 to 19 mg), Co-P (from 18 to 20 mg), Ni-Co (from 20 to 23 mg), and NiCoP (from 24 to 28 mg) catalysts prepared under a magnetic field were improved compared with those prepared without a magnetic field. The reasons for the

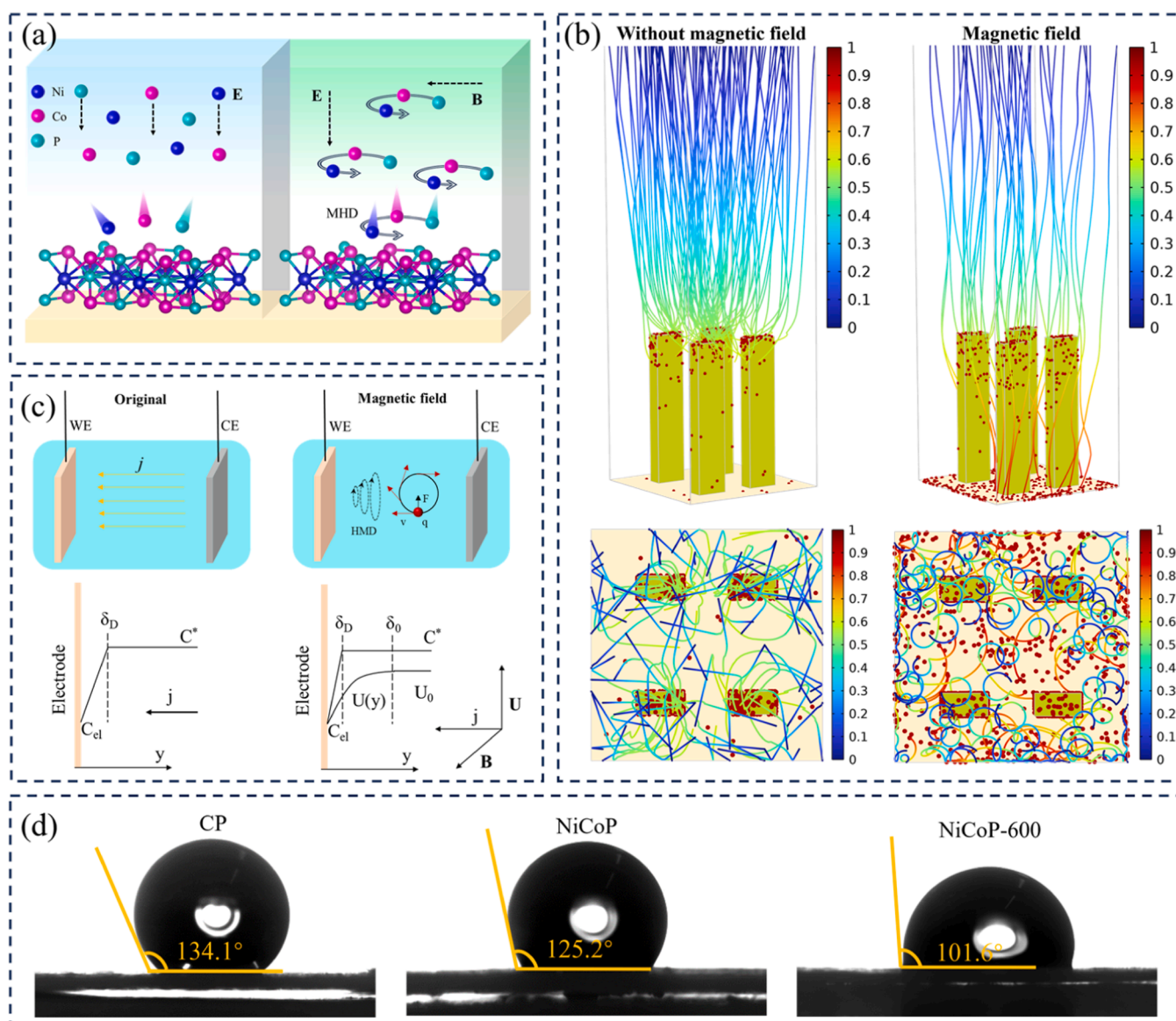


Fig. 2. (a) Ni, Co and P deposition diagram with or without magnetic field. (b) COMSOL simulates the trajectory distribution of charged particles near the bump with and without magnetic field. (c) The thickness of the diffusion layer on the catalyst surface with and without a magnetic field. (d) The wetting angle of an aqueous solution of CP, NiCoP and NiCoP-600.

promotion can be attributed to the following three factors. First, the magnetic field weakens the thickness of the diffusion layer and enhances the wetting ability. Fig. 2c shows that the MHD effect caused by the magnetic field weakens the diffusion layer thickness and increases the limiting current density (Fig. S20) [38]. At the same time, Fig. 2d and S21 show the water contact angles of CP, NiCoP, NiCoP-300, and NiCoP-600, which were 134.1°, 125.2°, 114.7°, and 101.6°, respectively. This result confirms that NiCoP-600 had better wettability, which may be beneficial to the reaction between active substances and catalyst surfaces. Second, the magnetic field reduced the concentration difference of the solution. Under electrodeposition without a magnetic field, Ni, Co, and P ions near the electrode surface were continuously consumed, which aggravated the concentration gradient [39]. However, when a magnetic field is applied, the MHD effect will accelerate the ion transport rate and replenish consumed ions over time (Fig. S22 and Video S1) [40]. Notably, in the process of NiCoP deposition, Co usually takes precedence over Ni, such that the relative content of Co is higher than that of Ni [41]. The inductive Coupled Plasma Emission Spectrometer (ICP) results of NiCoP and NiCoP-600 also confirmed that the magnetic field will accelerate the preferential deposition of Co. Third, the magnetic field inhibited bubble growth and promoted bubble detachment. In-situ observations of bubble size and motion trajectory during deposition were performed with a high-speed camera. Fig. S23 shows the bubbles on the catalyst surface with and without a magnetic field. The results clearly show that the coverage rate of bubbles on the catalyst surface was as high as 20.3 % without a magnetic field, and the average bubble size was 52 μm (Fig. S24). Remarkably, when a 600 mT magnetic field was applied, the bubble coverage rate on the catalyst surface decreased to 5.6 %, and the average bubble size decreased to 30 μm (Fig. S25), which increased the chance of more contact between active substances and the catalyst surface. The reason for the refinement of the bubbles can mainly be attributed to the change of the body force on the bubbles from the original vertical downward direction without a magnetic field to the center of the bubbles around the magnetic field

(Fig. S26). This transformation causes the cross-sectional area of the bubbles to become smaller [42]. The decrease in coverage mainly derives from the micro-rotation induced by the magnetic field around the bubble and the MHD effect accelerating the bubble detachment (Video S2) [43–45].

Supplementary material related to this article can be found online at [doi:10.1016/j.apcatb.2023.123579](https://doi.org/10.1016/j.apcatb.2023.123579).

Fig. 3a shows XRD patterns of CP, NiCoP, and NiCoP-600. For NiCoP and NiCoP-600 samples, a series of diffraction peaks at 40.9°, 44.8°, 47.5°, and 75.4° correspond to the (111), (201), (210), and (212) crystal planes of NiCoP (PDF # 71–2336) [46]. The diffraction peaks marked at 26.3° and 54.5° can be attributed to the (002) and (004) crystal planes of C (PDF # 41–1487) [47]. Additionally, the magnetic properties of NiCoP and NiCoP-600 were measured with a VSM, and the hysteresis loops are shown in Fig. 3b. The results show that the magnetic properties of NiCoP-600 were improved compared with those of NiCoP (Table S4). Notably, the magnetic properties of Ni-P-600, Co-P-600, and Ni-Co-600 were also enhanced compared with those of Ni-P, Co-P, and Ni-Co (Figs. S27–S29). The chemical valence states, surface electronic states, and elemental composition of the catalyst were studied us X-ray Photoelectron Spectroscopy (XPS). As shown in Fig. 3c, the peaks of Ni, Co, and P were clearly observed in the full spectra of NiCoP and NiCoP-600. As shown in Fig. 3d, the high-resolution spectrum of NiCoP-600 Ni 2p consisted of three pairs of bimodal peaks. The weak peaks at 870.1 and 852.9 eV are attributed to the Ni-P bond, the peaks at 873.9 and 856.2 eV derive from the Ni-O bond, and the peaks at 880.4 and 861.9 eV are satellite peaks [48,49]. Similarly, the Co 2p spectra shown in Fig. 3e, featured three pairs of peaks corresponding to Co-P (793.3 and 778.3 eV), Co-O (796.9 and 781.2 eV), and satellite peaks (803.4 and 785.1 eV), respectively. For the XPS spectrum of P 2p (Fig. 3f), the peak at 129.6 eV corresponds to the P-M bond. However, the peak at 133.1 eV was assigned to the P-O bond, which is caused by unavoidable oxidation of the surface [50]. Additionally, compared with the peaks in NiCoP, the Ni-P and Co-P bonds of NiCoP-600 moved to a

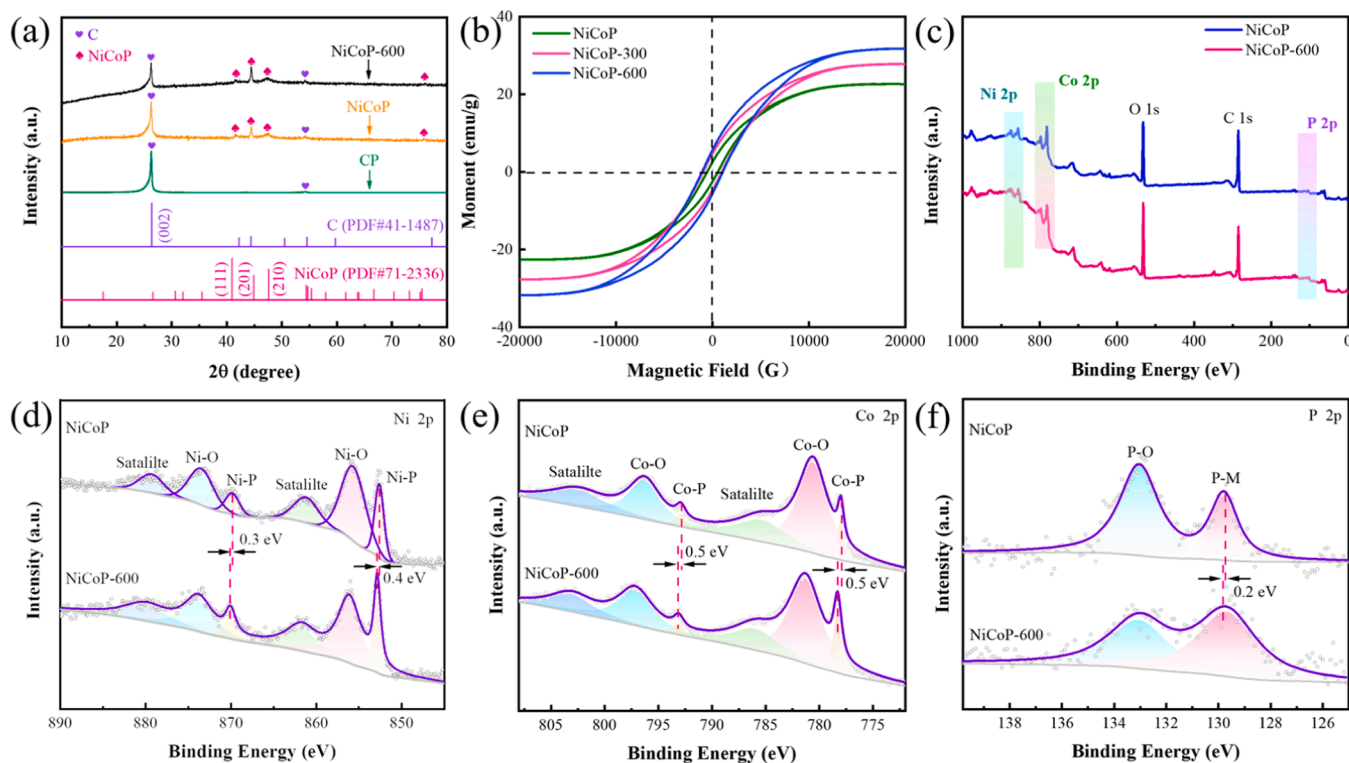


Fig. 3. (a) XRD patterns of CP, NiCoP and NiCoP-600. (b) Magnetic hysteresis loops of NiCoP, NiCoP-300 and NiCoP-600. (c) XPS survey spectra, (d) Ni 2p, (e) Co 2p, and (f) P 2p of NiCoP and NiCoP-600.

higher binding energy, whereas the P-M bond moved to a low binding energy. Specifically, the Ni-P bond of Ni 2p_{1/2} and Ni 2p_{3/2} orbitals positively shifted by 0.3 and 0.4 eV, respectively, the Co-P bond of Co 2p_{1/2} and Co 2p_{3/2} orbitals positively shifted by more than 0.5 eV, and the P-M bond of P 2p negatively shifted by 0.2 eV. The positive shifts in the binding energies of the Ni-P and Co-P bonds indicate improved electron transfer ability of NiCoP-600 [51]. The negative shift of the P-M bond energy indicates an increase in electron occupancy [52]. The above XPS results confirm that the introduction of a magnetic field during the preparation of NiCoP by electrodeposition can optimize the electron configuration and produce a higher electron distribution at Co and Ni sites, which is beneficial for HER performance [53].

As shown in the polarization curve of Fig. 4a, the hydrogen evolution performance of the catalyst was tested in 1.0 M KOH using a standard three-electrode system. The catalytic activities of CP, NiCoP, NiCoP-300, NiCoP-600, and Pt/C were compared. Fig. 4b shows that the overpotential values of NiCoP-600 were only 48, 81, and 92 mV at current densities of 10, 50, and 100 mA cm⁻², respectively, and were much lower than that of NiCoP (102, 142, and 166 mV) and NiCoP-300 (66, 109, and 127 mV),

109, and 127 mV). In the LSV of NiCoP-600 at high current was also measured (Fig. S30). The results showed that the overpotential of NiCoP-600 was only 232 mV when the current density was 500 mA cm⁻². Additionally, the linear sweep voltammetry (LSV) curves of NiCoP-600 in 0.5 M H₂SO₄ was tested. Remarkably, NiCoP-600 maintained excellent hydrogen evolution performance (Fig. S31). When the current density was 10 and 100 mA cm⁻², the overpotential of NiCoP-600 increased by 68.8 % (112–34 mV) and 47.7 % (214–112 mV), respectively, compared with that of NiCoP. The above results confirm that the hydrogen evolution activity of the catalysts prepared under MED was clearly enhanced. This enhancement is mainly attributed to the application of the magnetic field, which optimizes the Ni/Co deposition ratio and provides more active sites (Co).

To eliminate the mass loading effect as much as possible, the turnover frequency (TOF) was used to verify the intrinsic activity of NiCoP under a magnetic field [54]. NiCoP-600 exhibited a significant TOF of $2.5 \times 10^{-2} \text{ s}^{-1}$ at a potential of 100 mV (Fig. S32), 36 times higher than NiCoP ($6.9 \times 10^{-4} \text{ s}^{-1}$) and 12 times higher than NiCoP-300 ($2.1 \times 10^{-3} \text{ s}^{-1}$). Additionally, the Tafel slope of NiCoP-600 was only

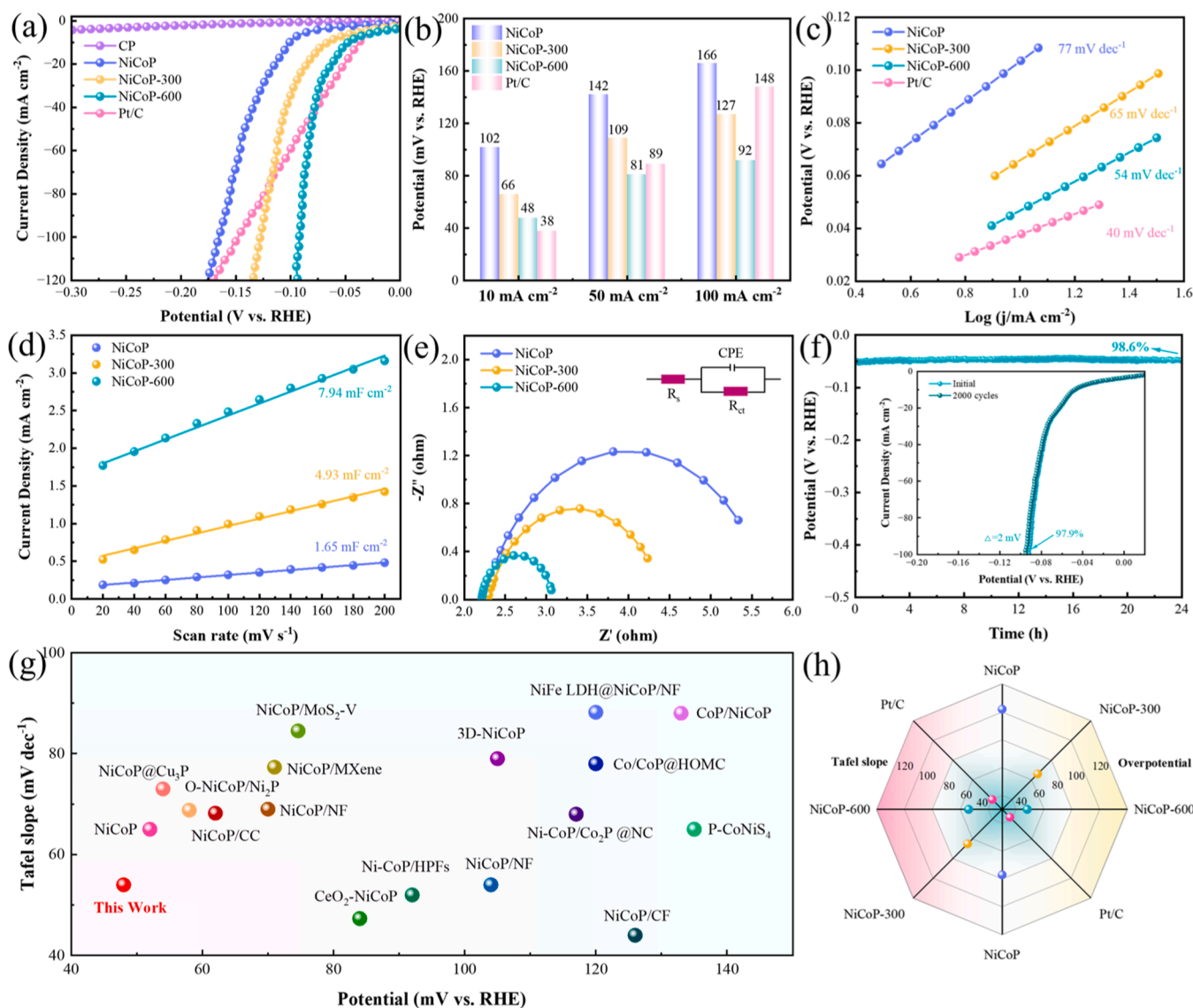


Fig. 4. (a-b) Polarization curves of CP, NiCoP, NiCoP-300, NiCoP-600, and Pt/C in 1 M KOH. (c) Tafel slopes of NiCoP, NiCoP-300, NiCoP-600, and Pt/C. (d) C_{dl} and (e) EIS Nyquist plots of NiCoP, NiCoP-300 and NiCoP-600. (f) Chronopotentiometry curve obtained from the NiCoP-600 at 10 mA cm⁻² (inset: Polarization curves acquired before and after 2000 cyclic voltammetry cycles). (g) The comparison in tafel slope and overpotential of NiCoP-600 with other reported HER catalysts in 1 M KOH. (h) The comparison in tafel slope and overpotential of NiCoP-600 with other reported HER catalysts in 1 M KOH.

54 mV dec⁻¹ (Fig. 4c), which is smaller than that of NiCoP (77 mV dec⁻¹) and NiCoP-300 (65 mV dec⁻¹), implying that NiCoP-600 has faster reaction kinetics and that the HER process follows the Volmer-Heyrovsky mechanism. Double-layer capacitance (C_{dl}) and electrochemical active surface area (ECSA) measurements were used to determine the number of active sites. As shown in Fig. 4d and S33, the ECSA values of NiCoP, NiCoP-300, and NiCoP-600 were 41.3, 123.3, and 198.5 cm², respectively. The C_{dl} and ECSA results indicate that the dense braided rope structure provides more active sites, which is consistent with the BET results. The ECSA value and current density normalization (J_{ECSA}) were used to evaluate the catalytic activity of samples per unit electrochemical active area. As expected, NiCoP-600 maintained high hydrogen evolution characteristics (Fig. S34). Additionally, the Nyquist diagrams for NiCoP, NiCoP-300, and NiCoP-600 are shown in Fig. 4e. Notably, NiCoP-600 had the smallest charge transfer impedance, which means that the dense braided rope structure and Co-rich Ni/Co ratio jointly promote the charge transfer [55].

Stability is the most critical index for the industrial application of catalysts. As shown in Fig. 4f-S35, NiCoP-600 was operated continuously for 24 h at a current density of 10 mA cm⁻², and its overpotential retention rate was as high as 98.6 % and 98.2 %. NiCoP-600 worked continuously for 24 h at a current density of 500 mA cm⁻² in 1 M KOH, and its overpotential retention rate was as high as 95.2 % (Fig. S36). In addition to the i-t test, the LSV curve of NiCoP-600 at 0.8–1.4 V for 2000 cycles was also tested. The results showed that the overpotential of the LSV curve decreased by only 2 mV at a current density of 100 mA cm⁻² after 2000 cycles, and the potential retention rate was as high as 97.9 %. The above tests show that NiCoP-600 has excellent long-term stability. NiCoP-600 samples from after the stability test were characterized by XRD, TEM, and XPS, as shown in Figs. S37-S39. These results show that the phase structure and morphology of NiCoP-600 were stable. The dense braided rope structure is the main reason for the stability of NiCoP-600 and effectively avoids catalyst shedding and agglomeration during long-term testing while also facilitating rapid detachment of bubbles. Fig. 4g shows a performance comparison between NiCoP-600 and currently reported NiCoP catalysts (Fig. S40 and Tables S5-S6). The radar chart shows that the HER activity of NiCoP-600 was

equivalent to that of Pt/C, which further confirms that NiCoP-600 is a promising HER catalyst (Fig. 4h).

To explore potential relationships between the magnetic field and HER performance, Ni-P, Co-P, and Ni-Co were prepared under magnetic fields of 0 and 600 mT, respectively. The phase and morphology of the Ni-P, Ni-P-600, Co-P, Co-P-600, Ni-Co, and Ni-Co-600 were analyzed by XRD, SEM, and TEM. Specifically, the morphology of Co-P formed without a magnetic field was nanoparticulate, whereas the morphology of Co-P-600 was angular and walnut-like with a refined particle size (Figs. S41-S43). Ni-Co formed with a walnut-shaped surface, whereas Ni-Co-600 had a burr-like cone-shaped surface (Figs. S44-S46). Ni-P had a granular morphology, whereas Ni-P-600 formed as a smooth film (Figs. S47-S49). LSV and EIS results also clearly showed that the catalyst prepared under a magnetic field had a lower overpotential and smaller charge transfer impedance in comparison with the catalyst formed without a magnetic field (Figs. S50-S52).

To elucidate the mechanism of HER of NiCoP under alkaline conditions, we calculated the reaction free energy using density functional theory (DFT) to study the influence of the catalyst interface on the alkaline HER kinetics. On the basis of analysis of XRD, TEM, and XPS results, NiCoP (201), Ni-P (111), and Co-P (101) crystal planes were used as the surface models for the theoretical calculations. Fig. 5a shows a differential charge density map of the NiCoP (201) crystal surface with adsorbed water molecules, which demonstrates an accumulation of charge at Co sites, implying interactions between Co and H₂O molecules. In an alkaline medium, the HERs of NiCoP, Ni-P, and Co-P follow the Volmer-Heyrovsky mechanism, which has three steps: (1) H₂O molecules adsorb at the interface of active sites to form H₂O*, (2) H₂O* dissociates into H-OH*, and (3) H* desorbs to form H₂ [56,57]. The adsorption models of H₂O* (Figs. S53-S55), H-OH*, and H* corresponding to this reaction process are shown in Figs. S56-S58. Generally, hydrogen adsorption-free energy (ΔG_{H^*}) is a key index to describe HER activity. A ΔG_{H^*} value closer to 0 indicates stronger catalytic activity [58]. As shown in Fig. 5b, the ΔG_{H^*} value of NiCoP is -0.25 eV, which is lower than that of Ni-P (-0.59 eV) and Co-P (-1.01 eV), indicating that the synergistic effect of Ni/Co is superior to the H* adsorption kinetics of Ni or Co at a single active site. The total density of states (DOS), partial

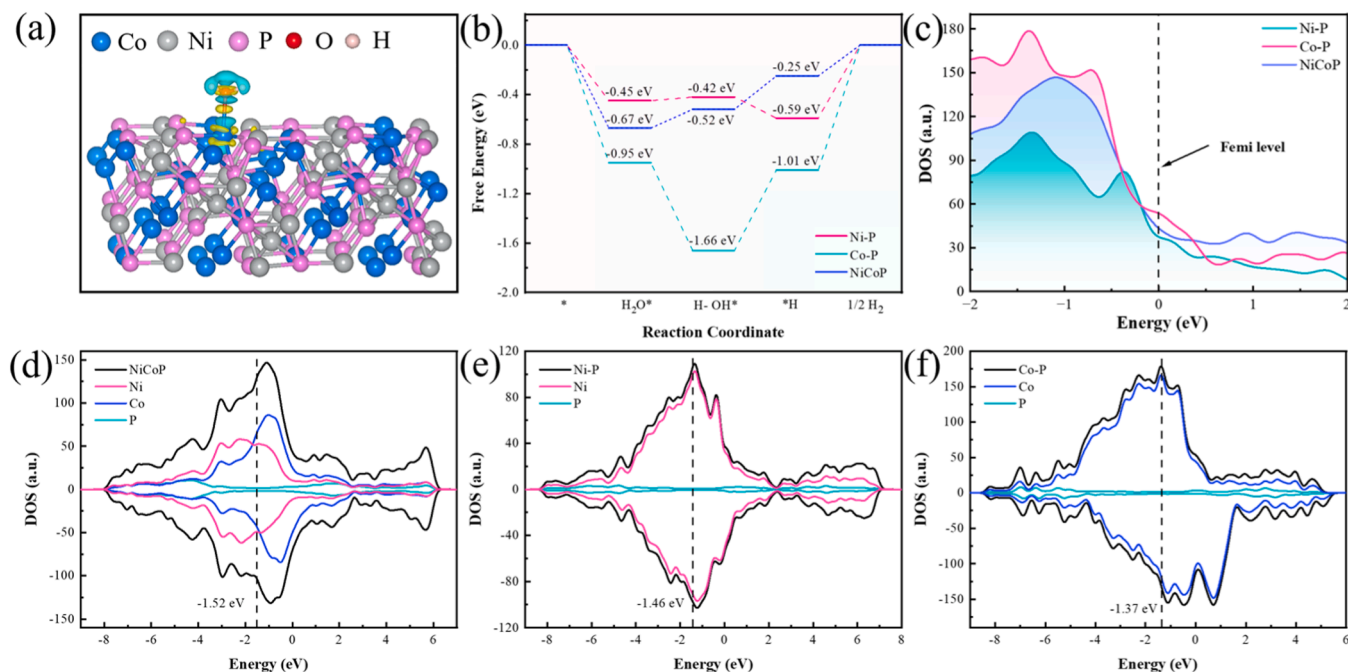


Fig. 5. (a) The charge density difference at the adsorption of H₂O on NiCoP with isovalue of the isosurfaces is $3.0 \times 10^{-3} e^{\text{Å}}$, and yellow (cyan) represents the charge accumulation (depletion). (b) Free energy for H₂O*, H-OH* and H* adsorptions in HER on the surfaces, (c) the density of states (DOS), and (d-f) the d-band center of Ni-P, Co-P and NiCoP.

density of states (PDOS), and d-band centers were calculated to further understand the electronic structure of the catalyst. As shown in Fig. 5c, near the Fermi level, the DOS value of NiCoP was higher than that of Ni-P and lower than that of Co-P, which indicates that an increase of the Co sites enhances the conductivity and fast electron transport ability of the catalyst. As shown in Fig. 5d-f, the DOS of NiCoP, Ni-P, and Co-P were continuous at the Fermi level, which also reflects the intrinsic metallic properties of the catalyst. Additionally, the d-band center of NiCoP (-1.52 eV) is farther from the Fermi level than that of Ni-P (-1.46 eV) or Co-P (-1.37 eV). According to d-band center theory, a d-band center far away from the Fermi level indicates that an anti-bonding band is filled by electrons with greater difficulty, and the

strength and stability of adsorbed bonds will be weakened [59,60]. Thus, the binding strength between the metal and adsorbate is decreased, which accelerates desorption of H^* from the catalyst surface and facilitates the rapid release of hydrogen.

Furthermore, the OER of NiCoP and NiCoP-600 were also measured in alkaline solution. As shown in Fig. 6a, the activity of NiCoP-600 increased by 13 % compared with that of NiCoP at a current density of 100 mA cm^{-2} . Furthermore, NiCoP-600 also showed faster reaction kinetics and lower electrochemical impedance (Fig. S59). As shown in Fig. S60, NiCoP-600 was operated continuously for 24 h at a current density of 10 mA cm^{-2} , and its overpotential retention rate was as high as 97.4 %. Fig. S61-S62 showed that the morphology of NiCoP after

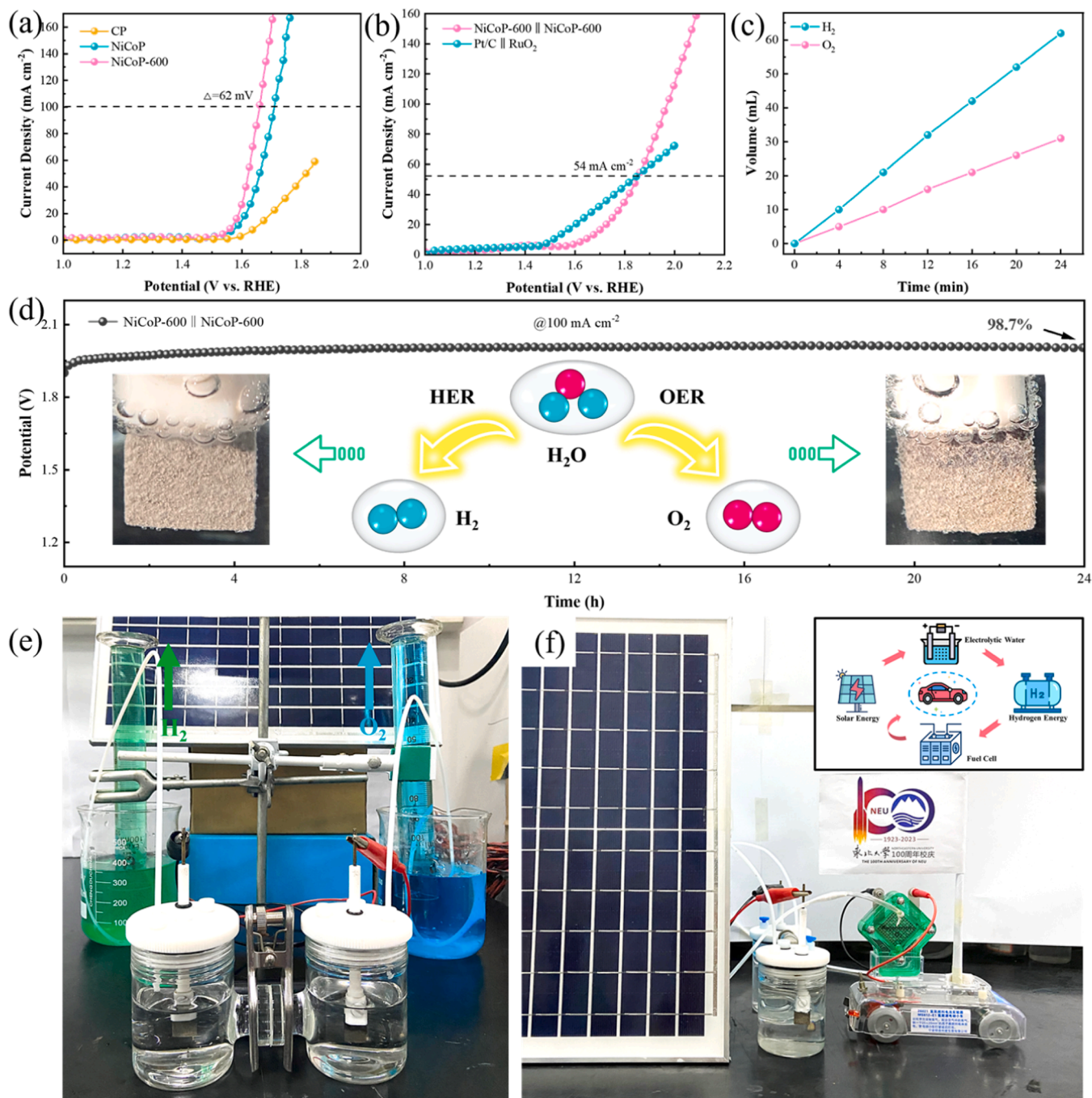


Fig. 6. Polarization curves of (a) CP, NiCoP and NiCoP-600, and (b) NiCoP-600||NiCoP-600 and Pt/C||RuO₂. (c) Amount of H₂ and O₂ as a function of time. (d) Chronopotentiometry curve of NiCoP-600||NiCoP-600 at 100 mA cm^{-2} . (e) H₂ and O₂ collection device of water splitting. (f) The green and clean energy-hydrogen system for overall water splitting in 1 M KOH.

stability test is still dense rope. The results confirm that NiCoP-600 can be used as a bifunctional catalyst in alkaline solution. Therefore, an H-type electrolytic cell was assembled, and NiCoP-600 was used as the cathode and anode. The LSV results show that NiCoP-600||NiCoP-600 outperformed Pt/C||RuO₂ at current densities greater than 54 mA cm⁻² (Fig. 6b and S63). The collection of H₂ and O₂ in total solution water were operated by the drainage method [61]. The gas changes in the measuring cylinder for 4, 8, 12, 16, 20, and 24 min were recorded during overall water splitting, and then the Faraday curve was drawn (Fig. 6c). The results show that 62 and 32 mL of H₂ and O₂ accumulated in the measuring cylinder, respectively, after 24 min, and the ratio was close to 2:1, which confirms that the Faraday efficiency of NiCoP-600 was close to 100 % (Figs. S64-S65). Fig. 6d shows that the NiCoP-600||NiCoP-600 couple can be maintained stably for 24 h at a current density of 100 mA cm⁻², with a potential retention of up to 98.7 %. To promote the scale-up and commercialization of hydrogen energy, we assembled solar panels to electrolyze water (Fig. 6e-f), and used the collected hydrogen to drive hydrogen fuel cell vehicles (Video S3). The successful development of these green and pollutant-free clean energy hydrogen production systems is expected to promote applications of NiCoP-600 in the electrolysis of water.

Supplementary material related to this article can be found online at [doi:10.1016/j.apcatb.2023.123579](https://doi.org/10.1016/j.apcatb.2023.123579).

4. Conclusion

In this work, NiCoP with a dense braided rope structure was prepared using the MED method as a high-efficiency electrocatalyst for HER. Compared with flower-like NiCoP prepared without a magnetic field, NiCoP-600 formed with a dense braided rope structure, which exhibited a larger electrochemical active area, faster electron transfer ability, and better hydrophilicity. Additionally, the magnetic field optimized the Ni/Co ratio, which was beneficial for exposing active sites. In summary, NiCoP-600 shows high efficiency and stability for HER activity in acidic or alkaline electrolytes. In 1.0 M KOH and 0.5 M H₂SO₄, respectively, the HER performance of NiCoP-600 reflects improvements of 45 % and 48 %, compared with that of NiCoP at a current density of 100 mA cm⁻². Additionally, NiCoP-600 also exhibits excellent water decomposition activity, and the required potential was 1.59 V at a current density of 10 mA cm⁻². Hence, this technology will greatly stimulate interest in the structural design of catalysts and optimization of active substances for high-efficiency HER catalysts.

CRediT authorship contribution statement

Zhong Wang: Methodology, Investigation, Writing - Original Draft; Hao Tian, Tuo Zang, Jinyang Li: Methodology, Investigation; Jiaqi Liu: Data Curation, Formal Analysis; Shuang Yuan: Resources, Supervision; Shuang Yuan, Guojian Li: Supervision; Jun Wang: Visualization, Review & Editing; Shuang Yuan: Conceptualization, Funding Acquisition, Review & Editing; Qiang Wang, Tie Liu: Funding Acquisition, Review & Editing.

Declaration of Competing Interest

The authors declared that they have no conflicts of interest to this work. We declare that we do not have any commercial or associative interest that represents a conflict of interest in connection with the work submitted.

Data availability

Data will be made available on request.

Acknowledgments

This work was financially supported by the National Natural Science Foundation of China (Grant No. 52274294), the Fundamental Research Funds for the Central Universities (Grant No. N2124007-1), the Fund of the State Key Laboratory of Solidification Processing in NWPU (Grant No. SKLSP202101). And we thank Liwen Bianji (Edanz) (www.liwenbianji.cn/) for editing the English text of a draft of this manuscript.

Appendix A. Supporting information

Supplementary data associated with this article can be found in the online version at [doi:10.1016/j.apcatb.2023.123579](https://doi.org/10.1016/j.apcatb.2023.123579).

References

- [1] Y. Zhou, S.J. Guo, Recent advances in cathode catalyst architecture for lithium-oxygen batteries, *eScience* 3 (2023), 100123, <https://doi.org/10.1016/j.esci.2023.100123>.
- [2] Y. Gu, A.P. Wu, Y.Q. Jiao, H.R. Zheng, X.Q. Wang, Y. Xie, L. Wang, C.G. Tian, H. G. Fu, Two-dimensional porous molybdenum phosphide/nitride heterojunction nanosheets for pH-universal hydrogen evolution reaction, *Angew. Chem. -Int. Ed.* 60 (2021) 6673–6681, <https://doi.org/10.1002/anie.202016102>.
- [3] S.C. Han, J.L. Quan, F.G. Zhou, Y.H. Xue, N. Li, F.Y. Li, D. Wang, 3D printing of architected graphene-based aerogels by cross-linking GO inks with adjustable viscoelasticity for energy storage devices, *Rare Met.* 42 (2023) 971–981, <https://doi.org/10.1007/s12598-022-02202-y>.
- [4] Y.P. Lei, Y.C. Wang, Y. Liu, C.Y. Song, Q. Li, D.S. Wang, Y.D. Li, Designing atomic active centers for hydrogen evolution electrocatalysts, *Angew. Chem. -Int. Ed.* 59 (2020) 20794–20812, <https://doi.org/10.1002/anie.201914647>.
- [5] R.L. Zhang, Y.Z. Li, X. Zhou, A. Yu, Q. Huang, T.T. Xu, L.T. Zhu, P. Peng, S.Y. Song, L. Echegoyen, F.F. Li, Single-atomic platinum on fullerene C₆₀ surfaces for accelerated alkaline hydrogen evolution, *Nat. Commun.* 14 (2023), 2460, <https://doi.org/10.1038/s41467-023-38126-z>.
- [6] S. Chakrabarti, S. Sinha, G.N. Tran, H. Na, L.M. Mirica, Characterization of paramagnetic states in an organometallic nickel hydrogen evolution electrocatalyst, *Nat. Commun.* 14 (2023), 905, <https://doi.org/10.1038/s41467-023-36609-7>.
- [7] W.L. Xu, R. Zhao, Q.Q. Li, B. Sun, J. Wu, W.D. Zhong, Y.H. Gao, X. Nan, Q. Huang, Y. Yang, X.K. Li, N.J. Yang, Q. Zhang, Overall water splitting on the NiS/NiS₂ heterostructures featuring self-equilibrium orbital occupancy, *Adv. Energy Mater.* (2023), 2300978, <https://doi.org/10.1002/aenm.202300978>.
- [8] X. Wang, M.H. Yu, X.L. Feng, Electronic structure regulation of noble metal-free materials toward alkaline oxygen electrocatalysis, *eScience* 3 (2023), 100141, <https://doi.org/10.1016/j.esci.2023.100141>.
- [9] Z.M. Sun, L. Lin, M.W. Yuan, H.Y. Yao, Y.J. Deng, B.B. Huang, H.F. Li, G.B. Sun, J. Zhu, Mott-schottky heterostructure induce the interfacial electron redistribution of MoS₂ for boosting pH-universal hydrogen evolution with Pt-like activity, *Nano Energy* 101 (2022), 107563, <https://doi.org/10.1016/j.nanoen.2022.107563>.
- [10] Z.X. Wu, Y. Zhao, W.P. Xiao, Y.L. Fu, B.H. Jia, T.Y. Ma, L. Wang, Metallic-bonded Pt-Co for atomically dispersed Pt in the Co₄N matrix as an efficient electrocatalyst for hydrogen generation, *ACS Nano* 16 (2022) 18038–18047, <https://doi.org/10.1021/acsnano.2c04090>.
- [11] M. Smiljanic, S. Panic, M. Bele, F. Ruiz-Zepeda, L. Pavko, L. Gasparic, A. Kokalj, M. Gabersek, N. Hodnik, Improving the HER activity and stability of Pt nanoparticles by titanium oxynitride support, *ACS Catal.* 12 (2022) 13021–13033, <https://doi.org/10.1021/acscatal.2c03214>.
- [12] Y.G. Zhao, N. Dongfang, C.A. Triana, C. Huang, R. Erni, W.C. Wan, J.G. Li, D. Stoian, L. Pan, P. Zhang, J.G. Lan, M. Iannuzzi, G.R. Patzke, Dynamics and control of active sites in hierarchically nanostructured cobalt phosphide/chalcogenide-based electrocatalysts for water splitting, *Energy Environ. Sci.* 15 (2022) 727–739, <https://doi.org/10.1039/D1EE02249K>.
- [13] L. Chen, Y.H. Song, Y. Liu, L. Xu, J.Q. Qin, Y.P. Lei, Y.G. Tang, NiCoP nanoleaves array for electrocatalytic alkaline H₂ evolution and overall water splitting, *J. Energy Chem.* 50 (2020) 395–401, <https://doi.org/10.1016/j.ijechem.2020.03.046>.
- [14] Q. Li, Y.C. Wang, J. Zeng, Q.M. Wu, Q.C. Wang, L. Sun, L. Xu, T. Ye, X. Zhao, L. Chen, Z.Y. Chen, L.M. Chen, Y.P. Lei, Phosphating-induced charge transfer on CoO/CoP interface for alkaline H₂ evolution, *Chin. Chem. Lett.* 32 (2021) 3355–3358, <https://doi.org/10.1016/j.cclet.2021.03.063>.
- [15] R. Zhang, Z.H. Wei, G.Y. Ye, G.J. Chen, J.J. Miao, X.H. Zhou, X.W. Zhu, X.Q. Cao, X.N. Sun, "d-electron complementation" induced V-Co phosphide for efficient overall water splitting, *Adv. Energy Mater.* 11 (2021), 2101758, <https://doi.org/10.1002/aenm.202101758>.
- [16] T. Liu, A.R. Li, C.B. Wang, W. Zhou, S.J. Liu, L. Guo, Interfacial electron transfer of Ni₂P-NiP₂ polymorphs inducing enhanced electrochemical properties, *Adv. Mater.* 30 (2018), 1803590, <https://doi.org/10.1002/adma.201803590>.
- [17] L.L. Ji, J.Y. Wang, X. Teng, T.J. Meyer, Z.F. Chen, CoP nanoframes as bifunctional electrocatalysts for efficient overall water splitting, *ACS Catal.* 10 (2020) 412–419, <https://doi.org/10.1021/acscatal.9b03623>.

- [18] W.Y. Fu, Y.X. Lin, M.S. Wang, S. Si, L. Wei, X.S. Zhao, Y.S. Wei, Sepaktakraw-like catalyst Mn-doped CoP enabling ultrastable electrocatalytic oxygen evolution at 100 mA cm⁻² in alkali media, *Rare Met.* 41 (2022) 3069–3077, <https://doi.org/10.1007/s12598-022-02006-0>.
- [19] S. Gupta, N. Patel, R. Fernandes, R. Kadrekar, A. Dashora, A.K. Yadav, D. Bhattacharyya, S.N. Jha, A. Miotello, D.C. Kothari, Co-Ni-B nanocatalyst for efficient hydrogen evolution reaction in wide pH range, *Appl. Catal. B-Environ.* 192 (2016) 126–133, <https://doi.org/10.1016/j.apcatb.2016.03.032>.
- [20] Y.W. Chen, L.X. Yang, C. Li, Y.Q. Wu, X. Lv, H.R. Wang, J.E. Qu, In situ hydrothermal oxidation of ternary FeCoNi alloy electrode for overall water splitting, *Energy Environ. Mater.* (2023), e12590, <https://doi.org/10.1002/eeem2.12590>.
- [21] J.J. Shen, B. Li, Y. Zheng, Z.Y. Dai, J.L. Li, X.Z. Bao, J.P. Guo, X.Q. Yu, Y. Guo, M. Z. Ge, W. Lei, H.Y. Shao, Engineering the composition and structure of superaerophobic nanosheet array for efficient hydrogen evolution, *Chem. Eng. J.* 433 (2022), 133517, <https://doi.org/10.1016/j.cej.2021.133517>.
- [22] M. Song, Z.J. Zhang, Q.W. Li, W. Jin, Z.X. Wu, G.T. Fu, X. Liu, Ni-foam supported Co(OH)F and Co-P nanoarrays for energy-efficient hydrogen production via urea electrolysis, *J. Mater. Chem. A* 7 (2019) 3697–3703, <https://doi.org/10.1039/C8TA10985K>.
- [23] Z. Wang, S. Yuan, J.Q. Liu, Y. Zhang, C. Liu, T. Liu, Q. Wang, Preparation of Ni₂P nanochains with controllable geometry for the hydrogen evolution reaction by application of a high magnetic field, *Scr. Mater.* 219 (2022), 114892, <https://doi.org/10.1016/j.scriptamat.2022.114892>.
- [24] W.D. Wang, J.V.I. Timonen, A. Carlson, D.M. Drotlef, C.T. Zhang, S. Kolbe, A. Grinthal, T.S. Wong, B. Hatton, S.H. Kang, S. Kennedy, J. Chi, R.T. Blough, M. Sitti, L. Mahadevan, J. Aizenberg, Multifunctional ferrofluid-infused surfaces with reconfigurable multiscale topography, *Nature* 559 (2018) 77–82, <https://doi.org/10.1038/s41586-018-0250-8>.
- [25] Y.C. Zhao, S.H. Gao, X. Zhang, W.X. Huo, H. Xu, C. Chen, J. Li, K.X. Xu, X. Huang, Fully flexible electromagnetic vibration sensors with annular field confinement origami magnetic membranes, *Adv. Funct. Mater.* 30 (2020), 2001553, <https://doi.org/10.1002/adfm.202001553>.
- [26] A.X. Wang, Q.B. Deng, L.J. Deng, X.Z. Guan, J.Y. Luo, Eliminating tip dendrite growth by lorentz force for stable lithium metal anodes, *Adv. Funct. Mater.* 29 (2019), 1902630, <https://doi.org/10.1002/adfm.201902630>.
- [27] C.W. Liang, P.C. Zou, A. Nairan, Y.Q. Zhang, J.X. Liu, K.W. Liu, S.Y. Hu, F.Y. Kang, H.J. Fan, C. Yang, Exceptional performance of hierarchical Ni-Fe oxyhydroxide@NiFe alloy nanowire array electrocatalysts for large current density water splitting, *Energy Environ. Sci.* 13 (2020) 86–95, <https://doi.org/10.1039/C9EE02388G>.
- [28] I. Bakonyi, L. Peter, Electrodeposited multilayer films with giant magnetoresistance (GMR): progress and problems, *Prog. Mater. Sci.* 55 (2010) 107–245, <https://doi.org/10.1016/j.pmatsci.2009.07.001>.
- [29] A.Y. Samardak, Y.S. Jeon, V.Y. Samardak, A.G. Kozlov, K.A. Rogachev, A.V. Ognev, E. Jeong, G.W. Kim, M.J. Ko, A.S. Samardak, Y.K. Kim, Interwire and intrawire magnetostatic interactions in Fe-Au barcode nanowires with alternating ferromagnetically strong and weak segments, *Small* 18 (2022), 2203555, <https://doi.org/10.1002/sml.202203555>.
- [30] M.Y. Huang, K. Skibinska, P. Zabinski, M. Wojnicki, G. Wloch, K. Eckert, G. Mutschke, On the prospects of magnetic-field-assisted electrodeposition of nanostructured ferromagnetic layers, *Electrochim. Acta* 420 (2022), 140422, <https://doi.org/10.1016/j.electacta.2022.140422>.
- [31] M. Uhlemann, K. Schulik, A. Gebert, G. Mutschke, J. Fröhlich, A. Bund, X.G. Yang, K. Eckert, Structured electrodeposition in magnetic gradient fields, *Eur. Phys. J. -Spec. Top.* 220 (2013) 287–302.
- [32] H. Li, S. Lin, H. Li, Z.Q. Wu, Q. Chen, L.L. Zhu, C.D. Li, X.B. Zhu, Y.P. Sun, Magneto-electrodeposition of 3D cross-linked NiCo-LDH for flexible high-performance supercapacitors, *Small Methods* 6 (2022), 2101320, <https://doi.org/10.1002/smt.202101320>.
- [33] C. Wei, Z.C.J. Xu, The possible implications of magnetic field effect on understanding the reactant of water splitting, *Chin. J. Catal.* 43 (2022) 148–157, [https://doi.org/10.1016/S1872-2067\(21\)63821-4](https://doi.org/10.1016/S1872-2067(21)63821-4).
- [34] Y. Wen, J.Y. Qi, D.Q. Zhao, J.H. Liu, P.C. Wei, X. Kang, X. Li, O doping hierarchical NiCoP/Ni₂P hybrid with modulated electron density for efficient alkaline hydrogen evolution reaction, *Appl. Catal. B-Environ.* 293 (2021), 120196, <https://doi.org/10.1016/j.apcatb.2021.120196>.
- [35] X.D. Ding, L.S. Pei, Y.X. Huang, D.Y. Chen, Z.L. Xie, Hollow NiCoP nanoprisms derived from prussian blue analogues as bifunctional electrocatalysts for urea-assisted hydrogen production in alkaline media, *Small* 18 (2022), 2205547, <https://doi.org/10.1002/sml.202205547>.
- [36] K. Shen, Z. Wang, X.X. Bi, Y. Ying, D. Zhang, C.B. Jin, G.Y. Hou, H.Z. Cao, L.K. Wu, G.Q. Zheng, Y.P. Tang, X.Y. Tao, J. Lu, Magnetic field-suppressed lithium dendrite growth for stable lithium-metal batteries, *Adv. Energy Mater.* 9 (2019), 1900260, <https://doi.org/10.1002/aenm.201900260>.
- [37] O. Aaboubi, K. Mselak, Magnetic field effects on the electrodeposition of CoNiMo alloys, *Appl. Surf. Sci.* 396 (2017) 375–383, <https://doi.org/10.1016/j.apsusc.2016.10.164>.
- [38] L. Liu, X. Yu, W.W. Zhang, Q.Y. Lv, L. Hou, Y. Fautrelle, Z.M. Ren, G.H. Cao, X. G. Lu, X. Li, Strong magnetic-field-engineered porous template for fabricating hierarchical porous Ni-Co-Zn-P nanoplate arrays as battery-type electrodes of advanced all-solid-state supercapacitors, *ACS Appl. Mater. Interfaces* 14 (2022) 2782–2793, <https://doi.org/10.1021/acsami.1c19997>.
- [39] M. Huang, G. Marinaro, X. Yang, B. Fritzsche, Z. Lei, M. Uhlemann, K. Eckert, G. Mutschke, Mass transfer and electrolyte flow during electrodeposition on a conically shaped electrode under the influence of a magnetic field, *J. Electroanal. Chem.* 842 (2019) 203–213, <https://doi.org/10.1016/j.jelechem.2019.04.043>.
- [40] G. Mutschke, A. Hess, A. Bund, J. Fröhlich, On the origin of horizontal counter-rotating electrolyte flow during copper magnetoelectrolysis, *Electrochim. Acta* 55 (2010) 1543–1547, <https://doi.org/10.1016/j.electacta.2009.10.015>.
- [41] W. Jiang, H.G. Li, Y.X. Lao, X. Li, M. Fang, Y.L. Chen, Synthesis and characterization of amorphous NiCoP alloy films by magnetic assisted jet electrodeposition, *J. Alloy. Compd.* 910 (2022), 164848, <https://doi.org/10.1016/j.jallcom.2022.164848>.
- [42] C.S. Zhu, Z. Hu, K.M. Wang, Multi-bubble motion behavior of uniform magnetic field based on phase field model, *Chin. Phys. B* 29 (2020), 034702, <https://doi.org/10.1088/1674-1056/ab6839>.
- [43] P. Liang, Q. Li, L.M. Chen, Z.J. Tang, Z.T. Li, Y. Wang, Y.C. Tang, C.P. Han, Z. W. Lan, C.Y. Zhi, H.F. Li, The magnetohydrodynamic effect enables a dendrite-free Zn anode in alkaline electrolytes, *J. Mater. Chem. A* 10 (2022) 11971–11979, <https://doi.org/10.1039/D2TA02077G>.
- [44] S. Takagi, T. Asada, Y. Oshikiri, M. Miura, R. Morimoto, A. Sugiyama, I. Mogi, R. Aogaki, Nanobubble formation from ionic vacancies in an electrode reaction on a fringed disk electrode under a uniform vertical magnetic field-2. Measurement of the angular velocity of a vertical magnetohydrodynamic (MHD) flow by the microbubbles originating from ionic vacancies, *J. Electroanal. Chem.* 916 (2022), 116375, <https://doi.org/10.1016/j.jelechem.2022.116375>.
- [45] Y. Liu, L.M. Pan, H.B. Liu, T.M. Chen, S.Y. Yin, M.M. Liu, Effects of magnetic field on water electrolysis using foam electrodes, *Int. J. Hydrogen Energy* 44 (2019) 1352–1358, <https://doi.org/10.1016/j.ijhydene.2018.11.103>.
- [46] X.X. Ma, Y.Q. Chang, Z. Zhang, J.L. Tang, Forest-like NiCoP@Cu₃P supported on copper foam as a bifunctional catalyst for efficient water splitting, *J. Mater. Chem. A* 6 (2018) 2100–2106, <https://doi.org/10.1039/C7TA09619D>.
- [47] J. Zhou, Y.B. Dou, T. He, X.J. Kong, L.H. Xie, J.R. Li, Encapsulation of bimetallic phosphides into graphitized carbon for pH-universal hydrogen evolution reaction, *J. Energy Chem.* 63 (2021) 253–261, <https://doi.org/10.1016/j.jechem.2021.03.039>.
- [48] L.F. Xiong, B. Wang, H.R. Cai, H.J. Hao, J. Li, T. Yang, S.C. Yang, Understanding the doping effect on hydrogen evolution activity of transition-metal phosphides: modeled with Ni₂P, *Appl. Catal. B-Environ.* 295 (2021), 120283, <https://doi.org/10.1016/j.apcatb.2021.120283>.
- [49] E.L. Hu, Y.F. Feng, J.W. Nai, D. Zhao, Y. Hu, X.W. Lou, Construction of hierarchical Ni-Co-P hollow nanobricks with oriented nanosheets for efficient overall water splitting, *Energy Environ. Sci.* 11 (2018) 872–880, <https://doi.org/10.1039/C8EE00076J>.
- [50] H.J. Niu, Y. Yan, S.S. Jiang, T. Liu, T. Sun, W. Zhou, L. Guo, J.H. Li, Interfaces decrease the alkaline hydrogen-evolution kinetics energy barrier on NiCoP/Ti₃C₂T_x MXene, *ACS Nano* 16 (2022) 11049–11058, <https://doi.org/10.1021/acsnano.2c03711>.
- [51] C.L. Liu, G. Zhang, L. Yu, J.H. Qu, H.J. Liu, Oxygen doping to optimize atomic hydrogen binding energy on NiCoP for highly efficient hydrogen evolution, *Small* 14 (2018), 1800421, <https://doi.org/10.1002/sml.201800421>.
- [52] X. Guo, M.G. Li, L.Y. Qiu, F.Y. Tian, L. He, S. Geng, Y.Q. Liu, Y. Song, W.W. Yang, Y.S. Yu, Engineering electron redistribution of bimetallic phosphates with CeO₂ enables high-performance overall water splitting, *Chem. Eng. J.* 453 (2023), 139796, <https://doi.org/10.1016/j.cej.2022.139796>.
- [53] T. Zhao, S.H. Wang, Y.B. Li, C. Jia, Z. Su, D.R. Hao, B.J. Ni, Q. Zhang, C.A. Zhao, Hierostructured V-doped Ni₂P/Ni₃P₂ electrocatalysts for hydrogen evolution in anion exchange membrane water electrolyzers, *Small* 18 (2022), 2204758, <https://doi.org/10.1002/sml.202204758>.
- [54] K. Wang, J.H. Zhou, M.Z. Sun, F.X. Lin, B.L. Huang, F. Lv, L.Y. Zeng, Q.H. Zhang, L. Gu, M.C. Luo, S.J. Guo, Cu-doped heterointerfaced Ru/RuSe₂ nanosheets with optimized H and H₂O adsorption boost hydrogen evolution catalysis, *Adv. Mater.* 35 (2023), 2300980, <https://doi.org/10.1002/adma.202300980>.
- [55] D. Chen, H.W. Bai, J.W. Zhu, C. Wu, H.Y. Zhao, D.L. Wu, J.X. Jiao, P.X. Ji, S.C. Mu, Multiscale hierarchical structured NiCoP enabling ampere-level water splitting for multi-scenarios green energy-to-hydrogen systems, *Adv. Energy Mater.* 13 (2023), 2300499, <https://doi.org/10.1002/aenm.202300499>.
- [56] D.K. Zhao, Z.L. Li, X.L. Yu, W. Zhou, Q.K. Wu, Y. Luo, N. Wang, A.M. Liu, L.G. Li, S. W. Chen, Ru decorated Co nanoparticles supported by N-doped carbon sheet implements Pt-like hydrogen evolution performance in wide pH range, *Chem. Eng. J.* 450 (2022), 138254, <https://doi.org/10.1016/j.cej.2022.138254>.
- [57] Z. Wang, S. Yuan, T. Zang, T.X. Li, Y.D. Zhou, J.Q. Liu, T. Liu, K. Wang, Q. Wang, Preparation of a Pt-Ni₂P/NF catalyst for highly efficient hydrogen evolution using a magnetic field to promote Ni-Pt galvanic replacement, *J. Mater. Sci. Technol.* 142 (2023) 144–151, <https://doi.org/10.1016/j.jmst.2022.09.030>.
- [58] D. Chen, R.H. Lu, R.H. Yu, H.Y. Zhao, D.L. Wu, Y.T. Yao, K.S. Yu, J.W. Zhu, P.X. Ji, Z.H. Pu, Z.K. Kou, J. Yu, J.S. Wu, S.C. Mu, Tuning active metal atomic spacing by filling of light atoms and resulting reversed hydrogen adsorption-distance relationship for efficient catalysis, *Nano-Micro Lett.* 15 (2023), 168, <https://doi.org/10.1007/s40820-023-01142-1>.
- [59] Y.J. Liu, Z. Li, H.X. Sun, L.J. Zheng, Z.S. Yuan, S.A. Li, Y.R. Li, X. Fang, Y.F. Gao, Z. Wang, X.P. Dai, X. Zhang, W.Y. Song, Trace N introduction accelerates desorption of intermediates for the HER and formation of MOOH species for the OER on NiCoP to boost overall water splitting, *J. Mater. Chem. A* 11 (2023) 1256–1267, <https://doi.org/10.1039/D2TA06897D>.
- [60] Q.Q. Li, F.Z. Huang, S.K. Li, H. Zhang, X.Y. Yu, Oxygen vacancy engineering synergistic with surface hydrophilicity modification of hollow Ru doped CoNi-LDH nanotube arrays for boosting hydrogen evolution, *Small* 18 (2022), 2104323, <https://doi.org/10.1002/sml.202104323>.
- [61] J.W. Zhu, Y. Guo, F. Liu, H.W. Xu, L. Gong, W.J. Shi, D. Chen, P.Y. Wang, Y. Yang, C.T. Zhang, J.S. Wu, J.H. Luo, S.C. Mu, Regulative electronic states around ruthenium/ruthenium disulfide heterointerfaces for efficient water splitting in

acidic media, Angew. Chem. -Int. Ed. 25 (2021) 12328–12334, <https://doi.org/10.1002/anie.202101539>.